

physica **p** status **s** solidi **S**

www.interscience.wiley.com

reprints

physica status solidi ^a
www.pss-a.com
applications and materials science
Editor's Choice
Highly efficient all-nitride phosphor-converted white light emitting diode
(Regina Mueller-Mach et al., p. 1727)
www.pss-a.com

physica status solidi ^b
www.pss-b.com
basic solid state physics
Current Trends in Electronic Structure: Embedding and Linear Scaling Techniques
Thomas Beck, and Eduardo Hernandez
www.pss-b.com

physica status solidi ^c
www.pss-c.com
current topics in solid state physics
SPECIAL ISSUE
www.pss-c.com

physica status solidi ^{rrl}
www.pss-rapid.com
rapid research letters
www.pss-rapid.com

physica status solidi ^{rapid}
www.pss-rapid.com
rapid research letters
www.pss-rapid.com

Anodic oxides on a beta type Nb–Ti alloy and their characterization by electrochemical impedance spectroscopy

Michael Teka Woldemedhin^{1,2}, Dierk Raabe¹, and Achim Walter Hassel^{*,1,2}

¹Max Planck Institut für Eisenforschung GmbH, Max-Planck-Str. 1, 40237 Düsseldorf, Germany

²Institute for Chemical Technology of Inorganic Materials, Johannes Kepler University, Altenbergerstr. 69, 4040 Linz, Austria

Received 14 October 2009, revised 7 March 2010, accepted 9 March 2010

Published online 8 April 2010

Keywords anodic oxides, electrochemical impedance spectroscopy, Mott–Schottky analysis, solid–liquid interface, β -Ti alloy

* Corresponding author: e-mail hassel@elchem.de, Phone: +43 732 2468 8704, Fax: +43 732 2468 8905

Anodic oxides were grown on the surface of an electropolished (Ti–30 at% Nb) beta-titanium (β -Ti) alloy by cyclic voltammetry. The scan rate was 100 mV s^{-1} between 0 and 8 V in increments of 1 V in an acetate buffer of pH 6.0. Electrochemical impedance spectroscopy was carried out right after each anodic oxide growth increment to study the electronic properties of the oxide/electrolyte interface in a wide frequency range from 100 kHz to 10 MHz with an AC perturbation voltage of 10 mV. A film formation factor of 2.4 nm V^{-1} was found and a relative permittivity number (dielectric constant) of 42.4 was deter-

mined for the oxide film formed. Mott–Schottky analysis on a potentiostatically formed 7 nm thick oxide film was performed to assess the semiconducting properties of the mixed anodic oxide grown on the alloy. A flat band potential of -0.47 V (standard hydrogen electrode, SHE) was determined, connected to a donor density of $8.2 \times 10^{17} \text{ cm}^{-3}$. β -Ti being highly isotropic in terms of mechanical properties should be superior to the stiffer α -Ti compound. Its application, however, requires a passivation behaviour comparable or better than α -Ti which in fact is found.

© 2010 WILEY-VCH Verlag GmbH & Co. KGaA, Weinheim

1 Introduction In a relatively short time Ti alloys found wide spread applications in aerospace, chemical industries, power plants, medical prostheses [1] and sporting goods [2] since their commercial inception in the early 1950s. Based on their crystalline structures Ti alloys are categorized into α -, ($\alpha + \beta$)- and β -type. The α -type is characterized by hexagonal closed packed (hcp) structure, β -type by body centred cubic (bcc) crystal structure and ($\alpha + \beta$)-type by a mixture of these two [3, 4].

β -type Ti alloys excel the other classes of Ti alloys for applications as biomaterials due their nontoxicity against osteoblastic cells, high-corrosion resistance and improved mechanical properties due to solid solution and second phase strengthening while preserving the light weight characteristics of titanium [4, 5]. The main advantage in using β -type Ti alloys is seen in the favourable mechanical properties. For crystallographic reasons, the body centred cubic structure shows higher symmetry as compared to the hcp α -Ti resulting in an isotropic mechanical behaviour. Further they have a low modulus of elasticity which makes them suitable for load bearing surgical implants where the aim consists in

providing replacement devices with stiffness similar to that of the human bone. This strategy lowers the load shielding effect which in current conventional implant alloy design (α -Ti) leads to bone decay followed by abrasion, infection and failure [4]. New processing methods may extend the range of application of established titanium alloys but only to a limited extent [6]. The potential of the alloy development is much higher.

The current Ti–30 at% Nb alloy is such a β -type alloy which is drawing considerable attention recently for the potential application as a biomaterial [7]. The second important point for using Ti-based alloys is their favourable passivation behaviour [8]. Ti is a reactive material and would undergo drastic dissolution but a dense and hard oxide layer forms that protect the material underneath efficiently from deterioration [9, 10]. The relative permittivity number of titanium oxide is around 40, which is similar to that of adsorbed water and one reason for the high biocompatibility of titanium. Other alloys such as the famous, nearly equiatomic, shape memory alloy NiTi form passive films which consist mainly of Ti despite the composition of the

alloy. In this way, leaching of nickel is hindered for the material in use and enables its application as a biomaterial [11].

Breme and Wadewitz [12] investigated various alloys Ti–Ta30 and Ti–Ta40, Ti–Nb40 and Ti–Nb50 and did not find significant differences in the corrosion behaviour in 0.9% saline solution.

Despite their potential application in this field, only few papers addressed the passivity and electronic properties of the oxides grown on such alloys. Semboshi et al. studied the structural and dielectric properties of anodic oxides films on Nb–Ti alloys with Ti contents in the alloy ranging from 0 to 15 at%. They found that the oxide films contained amorphous and partly crystalline niobium and titanium oxides. The increase of the titanium content in the alloy leads to an increase in the amount of titanium oxide in the mixed oxide film. The growing content of titanium oxide in the mixed alloy increases the capacitance of the mixed oxide film due to the higher dielectric number of the titanium oxide up to a composition of 3 at% Ti in the substrate alloy. Further increase in Ti content in the alloy beyond 3 at% decreases the capacitance due to the formation of a thicker oxide film which suppresses the effect of the higher dielectric number of the titanium oxide [13]. Metikos-Hukovic et al. studied the influence of niobium in the implant alloy Ti6Al6Nb on the stability of the oxide. They attributed the beneficial behaviour to the annihilation of anion vacancies in the titanium suboxide through the pentavalent niobium cation [14]. The versatility of the Nb–Ti–O system may be illustrated by an application for CO sensing by means of this system [15]. Mardare et al. [16] reported the high-throughput growth and characterization of anodic oxides on the surface of Ti–Nb thin film libraries where issues like the passivity of the surface and electrical properties of the anodic oxides grown were discussed for a large spread of alloys.

In this paper, a study of the passivity of a Ti–30 at% Nb β -Ti alloy surface and electronic properties of the mixed oxide are presented. With this regard electrochemical impedance spectroscopy (EIS) proves itself as a powerful tool in studying the oxide/electrolyte system.

2 Experimental

2.1 Sample preparation A metallurgically processed Ti–30 at% Nb sample [3, 4] of approximately 1 cm² area was mechanically ground with silicon carbide paper up to 2500 grit and then polished with silica slurry on a linen cloth. Finally, the sample was electropolished potentiostatically at 8 V and at a temperature of –10 °C in a water free solution of 3 M H₂SO₄ in methanol [17]. The sample was rinsed with distilled water, ultrasonicated in ethanol and dried in air after each procedure to remove leftovers from the preparation process.

2.2 Electrochemical experiments Cyclic voltammetry was used for the growth of anodic oxides on the samples surface in an acetate buffer of pH = 6.0. The potential was swept at a rate of 100 mV s^{–1} starting from 0 V

and reversal potentials varying in increments of 1 V up to a maximum potential of 8 V were used. Electrochemical impedance measurements were carried out right after each cyclic voltammetric scan from 100 kHz to 10 MHz frequency range with a perturbation AC voltage of 10 mV. For determining the flat band potential and the donor concentration, Mott–Schottky analysis was done on an oxide grown potentiostatically at 3 V for 1000 s. An Impedance/Gain-Phase Analyzer (Solartron SI 1260) coupled with a PAR Potentiostat/Galvanostat Model 283 (Princeton Applied research) was used for the electrochemical measurements. All the potentials in this paper are reported versus standard hydrogen electrode (SHE).

2.3 Electrochemical cell A double glass-walled cell with seven outlets, which were used for connecting the gas supply, counter, reference and working electrodes, was used for all the experiments. A commercial Ag/AgCl/3 M KCl (Metrohm) and gold plate of 2 cm² area were used as reference and counterelectrodes, respectively. The experiments were carried out at room temperature and the electrolyte was deaerated with Ar for 20 min prior to starting the experiments.

3 Results and discussion

3.1 Cyclic voltammetry Figure 1 shows the cyclic voltammograms for the anodic oxide formation on Ti–30 at% Nb sample. A sharp overshoot in current density is observed in the first cycle, which broadens and later disappears after the third cycle. The observed overshoot is a consequence of a delay in the growth of the oxide due to the build up of the space charge region as explained by the extended high-field model [18]. The current then falls and almost attains a constant current plateau till it reaches the upper oxide formation potential. During the reverse cathodic sweep of potential, the current falls rapidly towards zero. In the subsequent anodic sweep, the formation current stays to the minimum until it surpasses the formation potential of the

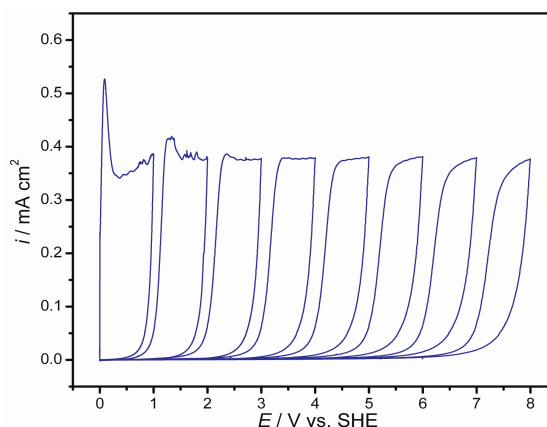


Figure 1 (online colour at: www.pss-a.com) Cyclic voltammograms from the anodic oxide growth on Ti–30 at% Nb in acetate buffer of pH 6.0. Potential is given with reference to the SHE.

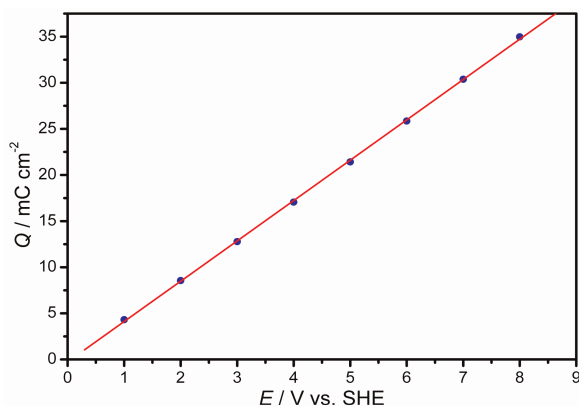


Figure 2 (online colour at: www.pss-a.com) Plot of charge consumed versus potential. Data are obtained by integration of the voltammograms shown in Fig. 1.

previously grown oxide. The growth of oxide becomes more and more retarded as the formation potential increases, evident from the increased gap between two subsequent curves as showing the voltammograms. The kinetic hindrance is also the reason behind for the smeared-out increase in the oxide formation current exhibited in the last three cycles [19].

A plot of the charge density (Q) versus the reversal potentials is shown in Fig. 2.

The slope of the linear fit of such a plot gives the oxide formation factor (k) which was calculated based on Eq. (1) to be 2.4 nm V^{-1}

$$d = \frac{MQ}{zrF\rho}, \quad (1)$$

where d is the oxide thickness, M the molecular weight, Q the charge density, z the number of exchanged electrons per formula unit, r the roughness factor which was assumed to be equal to one for an electropolished surface and ρ the density of the oxide [20].

This film formation factor is the reciprocal of the critical field strength of a certain oxide. Higher scan rates in the potential increase yield higher field strength up to the maximum scan rate of a potentiostatic experiment. Values of 2.6 nm V^{-1} for Ti and 2.8 nm V^{-1} for Nb have been found when the breakdown field strength of an anodic oxide is determined [21].

3.2 Electrochemical impedance spectroscopy Bode plot representation for impedance spectra obtained after each oxide growth increment during cyclic voltammetric measurements are shown in Fig. 3a and b. A near capacitive behaviour is observed with a phase shift close to -90° in the intermediate frequency range (10–100 Hz). The impedance in this region is almost only a contribution from the capacitive reactance which increases with the applied potential due to the oxide thickening as shown in Fig. 3a.

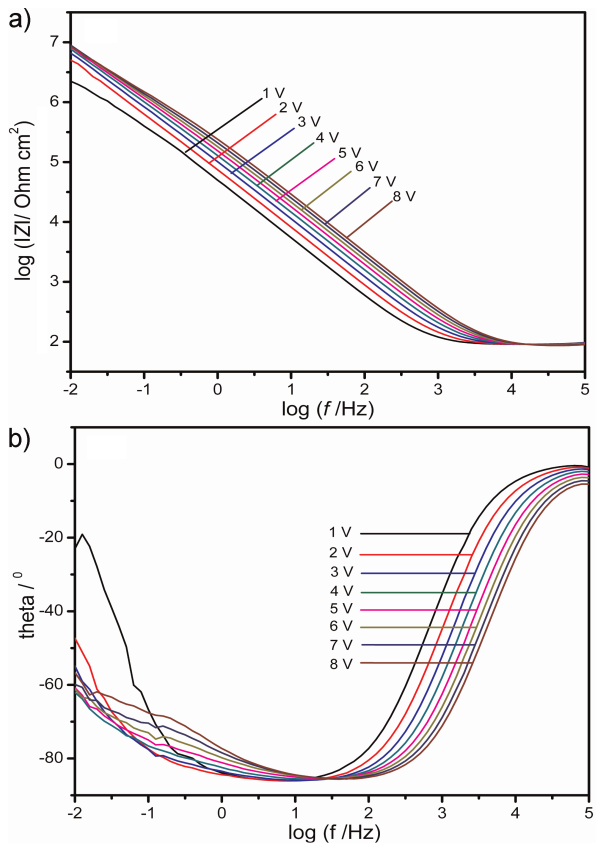


Figure 3 (online colour at: www.pss-a.com) (a,b) Bode plot representation of the EIS data of Ti-30 at% Nb during successive oxide growth.

Figure 4 shows the linear plot of C_{ox}^{-1} calculated from the impedance spectra versus the applied potential E . The relation between oxide capacitance C_{ox} and film thickness d can be written using the formula for a parallel plate condenser as:

$$C_{\text{ox}} = \frac{\epsilon_r \epsilon_0}{d}, \quad (2)$$

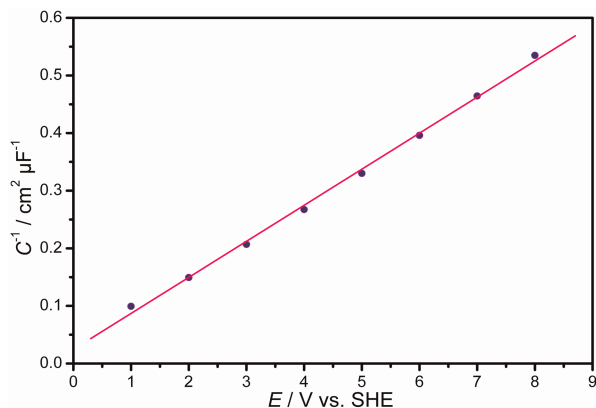


Figure 4 (online colour at: www.pss-a.com) Reciprocal capacitance of the oxide versus the formation potential.

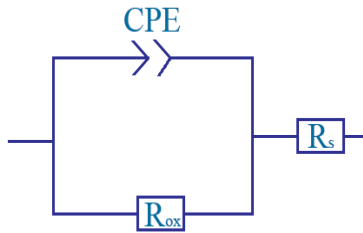


Figure 5 (online colour at: www.pss-a.com) Schematic drawing of the equivalent circuit used to simulate the oxide/electrolyte interface.

where ϵ_r is the relative permittivity number of the oxide, ϵ_0 the permittivity of vacuum and d the oxide thickness. The increment of oxide thickness with applied potential is given by:

$$d = k(E - E_{ox}), \quad (3)$$

where E_{ox} is the equilibrium potential of oxide electrode [11]. From the above two equations:

$$\frac{1}{C_{ox}} = \frac{k}{\epsilon_r \epsilon_0} (E - E_{ox}), \quad (4)$$

ϵ_r is determined to be 42.4 from the slope of Fig. 4 based on the value of k (2.4 nm V^{-1}) determined in the above section.

The equivalent circuit shown in Fig. 5 is used to fit the experimental curves. A constant phase element (CPE), connected parallel to the oxide resistance (R_{ox}) and in series with solution resistance (R_s), is used instead of an ideal capacitor. The impedance of the CPE is given by:

$$Z(\omega) = \frac{1}{Q} (j\omega)^{-n}, \quad (5)$$

where j is complex number, $0 < n < 1$ and Q is a constant. When $n = 1$, the CPE is acting like a perfect capacitor and when $n = 0$, the CPE becomes pure resistor [22]. The values of n obtained from fitting the experimental curves with the circuit shown below are in range of 0.92–0.97 indicating how much the CPE is close to being like an ideal capacitor.

Figure 6a and b shows the experimental and fitted curves obtained using this circuit model. Better fitting is obtained in whole frequency range for the impedance spectra of lower potentials, but deviation from the experimental curve is seen in the lower frequency range as the oxide is thickening at higher potentials.

3.3 Mott–Schottky analysis Mott–Schottky analysis was employed to study the semiconducting properties of the anodic oxide grown on the Ti–30 at% Nb sample, which relates the capacitance of the space charge region with the applied potential as:

$$C_{sc}^{-2} = \left(\frac{2}{e\epsilon_r\epsilon_0 N_D} \right) \left(E - E_{fb} - \frac{kT}{e} \right), \quad (6)$$

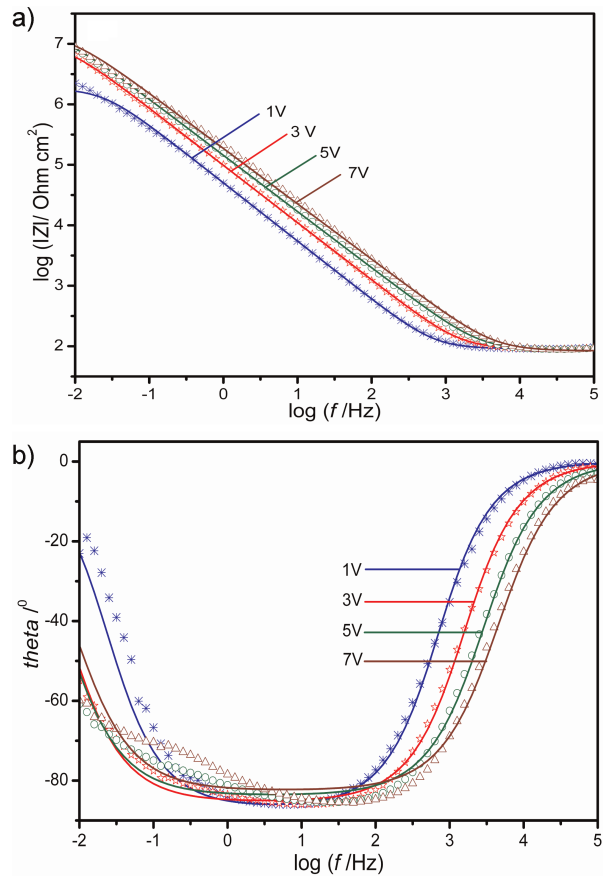


Figure 6 (online colour at: www.pss-a.com) (a,b) Bode plot for some of the experimental and fitted curves of the spectra. Symbols represent the experimental data and the solid lines fitted curves.

where e is the elementary charge, ϵ_r the relative permittivity of the oxide, ϵ_0 the permittivity of vacuum, N_D the donor concentration for an n -type semiconductor like the Ti–Nb investigated here, E_{fb} the flat band potential, k the Boltzmann constant and T the absolute temperature [23].

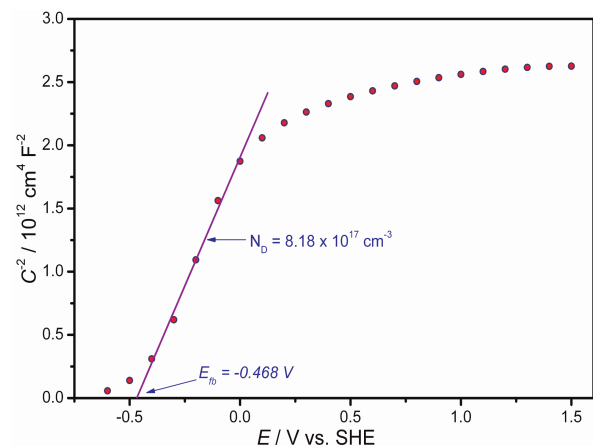


Figure 7 (online colour at: www.pss-a.com) Mott–Schottky plot for the potentiostatically grown oxide on the surface of Ti–30 at% Nb alloy.

For this purpose, an oxide was grown potentiostatically at 3 V for 1000 s. Then EIS was carried out at different bias potentials starting from 1.5 V and going down to -0.6 V in 100 mV steps in the frequency range from 10 kHz to 100 mHz. Variation of the capacitance of the space charge region which is calculated from the imaginary part of the impedance and the frequency where the phase shift reaches a maximum value versus applied potential is shown in Fig. 7. A linear region with a positive slope, indicating *n*-type semiconducting behaviour, is observed in the potential region of 0 to -0.4 V. The donor concentration and flat band potential are calculated, respectively, from the slope and intercept of the line fitted for this linear region as shown in Fig. 7. The Mott–Schottky evaluation yields donor density of $8.2 \times 10^{17} \text{ cm}^{-3}$ and E_{fb} equal to -0.47 V (SHE). The two values are lower than those reported by Mardare et al. [16] for thin film samples of the same composition.

The Ti–30 at% Nb alloy shows excellent passivity attributed to the continuous growth and thickening of the oxide with the applied potential. No side reactions such as oxygen evolution were noticed. But the results discussed so far were taken as net contributions from a large set of grains of polycrystalline Ti–30 at% Nb samples exposed to an acetate buffer electrolyte used in all of the experiments. Further experiments have to be conducted to elucidate the local electrochemical response at the single grain level of technically relevant polycrystalline samples. Crystallographic orientation of the grains determined by electron back scatter diffraction (EBSD) coupled with local microelectrochemical techniques with high-lateral resolution could give insight into the local electrochemical properties of polycrystalline samples. With this regard, efforts are underway in studying the passivation properties of single grains of a polycrystalline Ti–30 at% Nb sample using a scanning droplet cell where interesting differences are observed which will be reported in the near future. So far there are no hints on pinhole formation; both voltammograms and impedance spectra demonstrate the dense and stable nature of the forming oxide films. As for pure titanium and pure niobium, the high-field strength during oxide growth ensures an efficient removal of vacancies and the formation of a dry and water insoluble oxide.

The second aspect presently under investigation aims at understanding the structure and stability of the oxide formed. The breakdown potential is assumed to be a linear combination of those of the parent metals, as concluded from the voltammograms in this work. Depth profiles or angle resolved X-ray photoelectron spectroscopy should reveal whether or not a preferential transport of the cations during anodization yields a normal composition gradient.

4 Summary Anodic oxides on Ti–30 at% Nb grow according to the high-field mechanism as it is evident from the cyclic voltammograms obtained. They show an overshoot in current in the initial cycles which later change to current plateau in the intermediate cycles. The observed linear relationship between inverse of the oxide capacitance

and formation potential proves that the anodic oxide formed on this material is dielectric. The formation factor, one of the main parameters in the study of oxide films is determined from the charge consumed to grow the oxides. The dielectric property of the oxide is determined from the variation of the oxide capacitance, determined from the electrochemical impedance measurements, with formation potential. Mott–Schottky analysis carried out on potentiostatically formed oxide showed the *n*-type semiconducting properties of the mixed anodic oxide.

Acknowledgements M. T. Woldemedhin acknowledges the IMPRS-SurMat for a doctoral fellowship.

References

- [1] A. Cremasco, W. R. Osorio, C. M. A. Freire, A. Garcia, and R. Caram, *Electrochim. Acta* **53**, 4867 (2005).
- [2] C. R. M. Afonso, G. T. Aleixo, A. J. Ramirez, and R. Caram, *Mater. Sci. Eng. C* **27**, 908 (2007).
- [3] B. Sander and D. Raabe, *Mater. Sci. Eng. A* **479**, 236 (2008).
- [4] D. Raabe, B. Sander, M. Friak, D. Ma, and J. Neugebauer, *Acta Mater.* **55**, 4475 (2007).
- [5] M. Karthega, V. Raman, and N. Rajendran, *Acta Biomater.* **3**, 1019 (2007).
- [6] B. Baufeld and O. van der Biest, *Sci. Technol. Adv. Mater.* **10**, 015008 (2009).
- [7] D. H. Ping, C. Y. Cui, F. X. Yin, and Y. Yamabe-Mitarai, *Scr. Mater.* **54**, 1305 (2006).
- [8] S. Kudelka, A. Michaelis, J. W. Schultze, and E. Smailos, *Metalloberfläche* **50**, 369 (1996).
- [9] F. Di Quarto, S. Piazza, and C. Sunseri, *Electrochim. Acta* **38**, 29 (1993).
- [10] N. T. C. Oliveira, S. R. Biaggio, S. Piazza, C. Sunseri, and F. Di Quarto, *Electrochim. Acta* **49**, 4563 (2004).
- [11] A. W. Hassel, *Min. Invas. Ther. Allied Technol.* **13**, 1 (2004).
- [12] J. Brems and V. Wadewitz, *Int. J. Oral. Maxillofac. Implants* **4**, 113 (1989).
- [13] S. Semboshi, K. Bando, N. Ohtsu, Y. Shim, and T. J. Konno, *Thin Solid Films* **516**, 8613 (2008).
- [14] M. Metikos-Hukovic, A. Kwokal, and J. Piljac, *Biomaterials* **24**, 3765 (2003).
- [15] T. Anukunprasert, C. Saiwan, and E. Traversa, *Sci. Technol. Adv. Mater.* **6**, 359 (2005).
- [16] A. I. Mardare, A. Savan, A. Ludwig, A. D. Wieck, and A. W. Hassel, *Electrochim. Acta* **54**, 5973 (2009).
- [17] K. Fushimi, M. Stratmann, and A. W. Hassel, *Electrochim. Acta* **52**, 1290 (2006).
- [18] M. M. Lohrengel, *Mater. Sci. Eng. R* **11**, 243 (1993).
- [19] J. W. Schultze and A. W. Hassel, *Passivity of Metals, Alloys, and Semiconductors*, in: *Encyclopedia of Electrochemistry*, edited by A. J. Bard and M. Stratmann, Vol. 4, Corrosion and Oxide Films, edited by M. Stratmann and G. S. Frankel (Wiley-VCH, Weinheim, 2003), pp. 216–270 and 188–189.
- [20] J. W. Schultze and M. M. Lohrengel, *Electrochim. Acta* **45**, 2499 (2000).
- [21] A. W. Hassel and D. Diesing, *Thin Solid Films* **414**, 296 (2002).
- [22] J. Bisquet, G. Garcia-Belmonte, P. Bueno, E. Longo, and L. O. S. Bulhoes, *J. Electroanal. Chem.* **452**, 229 (1998).
- [23] R. Silva, M. A. Barbosa, B. Rondot, and M. Cunha Belo, *Br. Corros. J.* **25**, 136 (1990).